Direct Damping Feedback Control Using Power Electronics-Interfaced Resources

Xin Xu, *Student Member, IEEE*, Kai Sun, *Senior Member, IEEE*

***Abstract*—This paper proposes a direct damping feedback control method against power system oscillations under small or large disturbances. For a targeted oscillation mode, this control method continuously minimizes the difference between the real-time estimated damping ratio and a desired value by changing power outputs of selected inverter-based resources. The method adopts a proportional-integral controller whose parameters are tuned using a nonlinear single-input-single-output model on damping estimation and control with a single-oscillator equivalent regarding the targeted power system mode. Also, optimization of these controller parameters considers both robustness and time performance in damping control. The paper also proposes utilizing a "zero-th order" parametric resonance phenomenon to simplify the controller design. Tests on a small power system and a 140-bus 48-machine Northeast Power Coordinating Council system validate the effectiveness of the proposed damping controller utilizing battery-based energy storage systems.**

***Index Terms*—Damping control, nonlinear modal decoupling, power system oscillation, power electronics-interfaced resource, inverter-based resources, battery based energy storage system, robust control.**

I. Introduction

MORE and more distributed energy resources (DERs) are integrated into power grids such as wind generators [1], [2], solar farms [3], [4], energy storage devices [5], etc., and are changing dynamic characteristics of power grids that used to be dominated by conventional synchronous generators. New operational concerns arise such as frequency excursions due to the decreased system inertia and more recurrent appearances of power system oscillations [6]. On the other hand, the DERs that are connected to the grid through power electronic devices also enable new control measures due to their more flexible and responsive control of power compared to synchronous generators.

The paper focuses on damping control of power system oscillation utilizing power electronics-interfaced resources (PEIRs) such as battery-based energy storage systems (BESS) and other inverter-based resources. In today's power grids, damping control are mainly undertaken by the power system stabilizer (PSS) with selected generators. The basic function of a PSS is to provide an auxiliary signal to the excitation control system of each selected generator to increase the damping torque of the rotor [7]. A typical PSS receives a measured or estimated rotor speed as the input signal. It employs a gain for the desired damping, a phase-lead component to compensate the phase lag with the exciter and a washout filter for a satisfactory steady-state performance. The tuning of the PSS aims to add a damping torque, i.e. an electric torque in phase with the rotor speed deviation, so as to increase damping ratios with a range of oscillation frequencies centered at a targeted oscillation mode. The targeted mode is usually an inter-area mode and might lead to a stability issue if lasting long and poorly damped. PSS-based damping control has been extended to wide-area applications that directly or indirectly tune the eigenvalues regarding the concerned modes by optimization techniques [8]-[12]. However, such a phase-compensation based control is incapable of fine control of damping ratio for a targeted mode.

The increasing deployment of DERs, especially PEIRs, enables an alternative, more straightforward damping control. In fact, a PEIR can provide oscillation damping by directly controlling its active power injected to the grid that is in phase with a measured frequency deviation. Many research activities have investigated damping control utilizing PEIRs. Papers [13] and [14] consider changing the power output of BESS to increase the damping ratio of a targeted mode to an expected value. Ref. [15] considers the superconducting magnetic energy storage and designs a close-loop control system to tune the eigenvalues of targeted modes. Ref. [16] uses a two-machine system to investigate impacts of the voltage-source-converters on damping in terms of placement and active/reactive power modulation. Ref. [17] proposes particle swarm optimization and heuristic dynamic programming based methods to adaptively control energy storage devices in order to stabilize the oscillation between two interconnected power systems.

Many of the existing PSS or PEIR based damping control methods design and tune their controllers by off-line studies on grid models regarding typical operating conditions. Then, when implemented in the real-time operating environment, the performance of an offline designed controller depends on how well a practical condition matches its offline assumptions and grid model. When the system undergoes a permanent topological change, the grid model used for the offline controller design becomes inaccurate. To cope with varying system conditions, more adaptive control strategies have been proposed for better online performance. For instance, ref. [18] uses a Federated Kalman Filter to online determine the most suitable damping controller among offline designed candidates for different

This work was supported in part by NSF grants ECCS-1553863 and in part by the ERC Program of the NSF and DOE under grant EEC-1041877.

X. Xu and K. Sun are with the Department of EECS, University of Tennessee, Knoxville, TN 37996 USA (e-mail: xxu30@vols.utk.edu, kaisun@utk.edu).

scenarios. Ref. [19] proposes adaptive coordination of damping controllers for the best dynamic performance. Besides, even with adaptivity being considered, most of existing methods are unable to do fine control of the damping ratio to a desired value; rather, they are open-loop and aim at an increase of damping. Thus, the damping ratio is either under-controlled to fail in reaching a desired threshold for some condition or over-controlled against the worse scenario so as to sacrifice the economical or dynamical performance of the grid.

In this paper, a PEIR-based direct damping feedback control method is proposed to address the aforementioned drawbacks of many existing damping controllers. The new control method targets at the modes of inter-area oscillations that might become poorly-damped under disturbances. By continuously changing the power injection from one or multiple PEIRs such as BESS, it can control the real-time damping ratio to follow closely a preset value even under a change of the operating condition. The proposed control system employs a closed-loop controller on a single-input-single-output (SISO) model that integrates two parts: a power system equivalent and a real-time damping estimation algorithm. The former is a reduced power system model that captures how the power injection from each of participating PEIRs changes system dynamics regarding the targeted mode and the latter provides the real-time estimated damping ratio to be directly fed back to the controller. This closed-loop feedback control can tolerate moderate mismatches between the power system equivalent and the real-time system condition and adjust the damping ratio continuously to a desired value. The fast power controls of PEIRs ensures the time performance of damping control. Furthermore, for a robust damping controller, this paper presents a design approach by identification of the transfer function of the SISO model based on a "zero-th order" parametric resonance phenomenon [20]. Using a PI (proportional-integral) controller as an example, the paper presents the detailed parameter tuning procedure considering both damping following performance under disturbances and robust control against errors in models or damping estimation.

In the rest of the paper, the proposed damping control method is presented in section II. The identification of the transfer function for the SISO model is presented in section III. How to design parameters for a robust PI controller is discussed in section IV. Section V illustrates the basic ideas of proposed method on an SMIB (single-machine-infinite-bus) system. Then, in section VI, a more realistic, 48-machine Northeast Power Coordinating Council (NPCC) test system is used to demonstrate the complete designing process and to validate effectiveness of the proposed controller. Finally, conclusions and future work are summarized in section VII.

II. Direct Damping Feedback Control System

The proposed direct damping feedback control system is illustrated in Fig. 1, including two blocks: *i*) the controller and *ii*) the SISO model representing the reduced power system regarding the targeted mode.

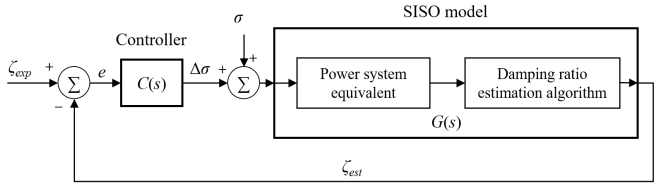

Fig. 1. Closed loop control system.

i) The controller $C(s)$ is the core of the proposed control system, whose goal is to eliminate the error e between the real-time estimated damping ratio ζ_{est} and the desired value ζ_{exp} for a targeted mode. In this paper a PI controller is used in the form of $\alpha_p + \alpha_i/s$, of which α_p and α_i are to be optimized considering both robustness and time performance.

ii) The SISO model described by a transfer function $G(s)$ consists of two parts, a power system equivalent receiving the system configuration input σ and the control input $\Delta\sigma$ from the controller, and then, a real-time damping estimation algorithm providing real-time estimated damping ratio ζ_{est}. σ corresponds to the damping induced from the system parameters, and $\Delta\sigma$ corresponds to the damping increase contributed by the controller. Note that the power system equivalent is only used to approximate the modal dynamics of the power system regarding the targeted mode during the stage of designing the entire control system; after the entire control system is implemented in real time, the signal $\Delta\sigma$ is fed to PEIRs participating in damping control. The SISO model can be approximated by a linear transfer function $G(s)$ based on the "zero-th order" parametric resonance.

The damping estimation function in the SISO model needs to adopt a measurement-based damping estimation algorithm that can provide real-time damping ratio for the targeted mode. Since this proposed control system faces both small and large disturbances, an algorithm that can use a short sliding time window is preferred. In this paper, the nonlinear oscillator fitting based damping estimation approach proposed in [21] is used for accurate and robust damping ratio estimation over short measuring windows. The approach inherits the idea of the nonlinear model decoupling (NMD) method, i.e. a coupled multi-oscillators system can be decoupled into a set of independent nonlinear 1-degree-of-freedom (1-DOF) oscillators, and each oscillator corresponds to a single oscillation mode [22]-[24]. Specifically, the response of the targeted mode is extracted into the modal space after a linear transformation, and then, it is fit into a nonlinear oscillator and the damping ratio can be calculated from the identified coefficients of the oscillator. Compared to linear system theory based damping estimation methods such as Prony's method and its variants [25], the damping estimation approach in [21] is less sensitive to the length and starting point of the measuring time window, especially for a short time window of, e.g., 3-5 seconds. When the power system behaves not exactly like a linear system subject to a large disturbance or control action, that damping estimation approach can provide an accurate, continuous estimate of the damping ratio. This feature is important for the proposed direct damping feedback control method in this paper.

A procedure for designing a robust PI damping controller will be proposed to address both expectations and determine the optimal control parameters α_p and α_i in the controller design stage. Once α_p and α_i are selected, the controller will keep operating with the power system. The damping ratio is estimated over a short sliding time window of ambient data with load variations or event data under a disturbance. The control system changes $\Delta\sigma$ to eliminate the deviation in the damping ratio from the expected value.

The proposed damping control system can be implemented in either a centralized or a decentralized manner. For a centralized control strategy, its core algorithms are installed at a central computer located, e.g., in the system control room, which receives wide-area measurements in order to perform damping estimation and sends control signals through communication channels to the participating PEIRs for actuation of damping control. On the other hand, in a decentralized control strategy, each participating PEIR has the proposed control system installed locally, performs damping estimation on the targeted mode, determines its control action, and coordinates with other PEIRs if needed. Later in Section IV-B, coordination among PEIRs will be discussed, including but not limited to ranking and activating PEIRs by their effectiveness in damping control and checking the control limit of each activated PEIR to determine whether a next PEIR needs to be activated and used.

The following two sections will first present the methods of the SISO model and then propose the robust PI controller.

III. Power System SISO Model

The purpose of this model is the equivalence of a power system's real-time dynamics regarding a targeted mode into a transfer function from the input $\sigma+\Delta\sigma$ to the output ζ_{est}. Such a transfer function will be included in the proposed control system so that a robust PI controller can be designed. To achieve such an objective, this section first reduces the power system to a single oscillator equivalent by the eigenvalue decomposition method and then derives the transfer function.

A. Power System Equivalence on the Targeted mode

The power electronic converter of a PEIR allows fast control of its voltage and power outputs according to expected values. Like FACTS (Flexible AC Transmission System) devices, a PEIR can utilize its voltage and reactive power control functions to increase oscillation damping if placed at some critical locations, which are typically on the oscillation path of the targeted mode [26]. For a PEIR that is able to control its active power output, such as a BESS, it can directly add damping to a targeted mode as demonstrated in [13]. Without loss of generality, this paper focuses on active power control of PEIRs, denoted by vector $\Delta\mathbf{P}_C$. The same approach and similar derivation steps can be easily applied to damping control by using reactive power or voltage outputs of a PEIR.

For a single PEIR, assume its active power output ΔP_C to follow this control law in the frequency domain [6]:

$$\Delta P_C(s) = -kF(s)\Delta\omega_C(s) \tag{1}$$

where k is a gain and F(s) is a transfer functions describing the internal control algorithm of PEIR. $\Delta\omega_C$ is the bus frequency deviation measured locally at the PEIR. The gain k will be tuned to provide desired damping. $F(s)$ depends on the type of the PEIR to be used and its capability in tuning its power output. For instance, a BESS is used in [14] following a control law shown in Fig. 2, where T_{BESS} (about tens of milliseconds) is the time constant of the BESS. For a power system with a number (denoted by L) of PEIRs to participate in the proposed damping control method, a damping distribution module (DDM), which receives $\Delta\sigma$ as its input and coordinates multiple gains, i.e. elements (denoted by k_l, l=1, …, L) of vector $\mathbf{k}$. When $\Delta\sigma$ is changed, the gains in $\mathbf{k}$ will be updated in real-time by DDM. This module will be discussed later in this subsection.

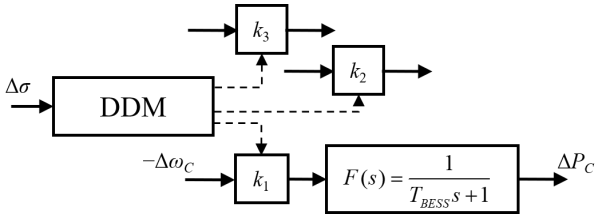

Fig. 2. Damping Distribution Module (DDM) with L=3.

When multiple PEIRs are considered, control law (1) can be generalized as

$$\Delta\mathbf{P}_C(s) = -diag(\mathbf{k})diag(\mathbf{F}(s))\Delta\boldsymbol{\omega}_C(s) \tag{2}$$

where $\mathbf{k}$, $\mathbf{F}$(s) and $\Delta\boldsymbol{\omega}_C$ are the vectors of all PEIRs' gains, transfer functions, and local bus frequency deviations, respectively. $diag(\cdot)$ is the operator to generate a diagonal matrix from a vector. Due to the capacity limits of the PEIR, the upper and lower bounds of $\mathbf{k}$ need to be determined.

$\Delta\mathbf{P}_C$ will result in changes of electrical powers of the generators, which are denoted by a vector $\Delta\mathbf{P}_e$. By linearization and Kron reduction techniques [7], $\Delta\mathbf{P}_e$ is approximated by

$$\Delta\mathbf{P}_e = \boldsymbol{\kappa}_1\Delta\mathbf{E}'_d + \boldsymbol{\kappa}_2\Delta\mathbf{E}'_q + \boldsymbol{\kappa}_3\Delta\boldsymbol{\delta} + \boldsymbol{\kappa}_4\Delta\mathbf{P}_C \tag{3}$$

where $\mathbf{E}'_d$ and $\mathbf{E}'_q$ are the transient voltages along the d and q axes, respectively. $\boldsymbol{\kappa}_i$ is the resulting coefficient matrix. The detailed steps to derive (3) can be found in Appendix A.

Bus frequency deviations $\Delta\boldsymbol{\omega}_C$ can be approximated by a linear function of the generator speed deviation $\Delta\boldsymbol{\omega}_G$. The network equations can be obtained by Kron reduction techniques on generator buses and PEIR buses:

$$\begin{bmatrix}\mathbf{I}_G\\ \mathbf{I}_C\end{bmatrix} = \begin{bmatrix}\mathbf{Y}_{GG} & \mathbf{Y}_{GC}\\ \mathbf{Y}_{CG} & \mathbf{Y}_{CC}\end{bmatrix}\begin{bmatrix}\mathbf{V}_G\\ \mathbf{V}_C\end{bmatrix} \tag{4}$$

where $\mathbf{I}$, $\mathbf{V}$, and $\mathbf{Y}$ are the current injection phasor, node voltage phasor, and the network impedance. The subscript "G" denotes the generator terminal buses, and "C" denotes the buses with PEIRs. Each V_i can be expressed in the polar coordinates $V_i = |V_i|e^{j\theta_i}$. For the generator buses, eq. (5) holds, where δ_j is the rotor angle and θ_{Gdqj} is the phase angle in the rotating d-q coordinates.

$$\theta_{Gj} = \delta_j - \pi/2 + \theta_{Gdqj} \tag{5}$$

The active powers at the PEIR buses are computed by (6), where Re(·) is the operator to extract the real part.

$$\mathbf{P}_C = \mathrm{Re}\left(diag(\mathbf{V}_C)\left(\mathbf{Y}^*_{CG}\mathbf{V}^*_G + \mathbf{Y}^*_{CC}\mathbf{V}^*_C\right)\right) \tag{6}$$

Eq. (7) can be derived from (6), according to (5), the assumptions listed below, and the linearization techniques.

i) All the conductances are omitted, i.e. $\mathbf{G}_{CG} = 0$ and $\mathbf{G}_{CC} = 0$;
ii) $\sin(\underline{\theta}_{Ci} - \theta_{Gj}) \approx \theta_{Ci} - \theta_{Gj}$ and $\sin(\theta_{Ci} - \theta_{Cj}) \approx \theta_{Ci} - \theta_{Cj}$;
iii) $|V_{Ci}| = |V_{Gi}| \approx 1$;
iv) $\dot{\theta}_{Gdqi} = 0$.

$$\Delta\dot{\mathbf{P}}_C = \mathbf{B}_{CC}\Delta\boldsymbol{\omega}_C - \mathbf{B}_{CG}\Delta\boldsymbol{\omega}_G \tag{7}$$

where $\mathbf{B}_{CC}$ and $\mathbf{B}_{CG}$ are susceptance matrices.

If the derivative of $\Delta\mathbf{P}_C$ is negligible, eq. (7) becomes:

$$\Delta\boldsymbol{\omega}_C = \mathbf{B}_{CC}^{-1}\mathbf{B}_{CG}\Delta\boldsymbol{\omega}_G \tag{8}$$

An alternative way to derive the function between $\Delta\boldsymbol{\omega}_G$ and $\Delta\boldsymbol{\omega}_C$ is introduced in [27], named as frequency divider, which is similar to (8) but the local load changes are not considered during the derivation. As shown later in the NPCC case studies, the approximation by (8) is acceptable for control performance.

With (2), (3) and (8) being considered, the linearized system model in the state space state vector $\Delta\mathbf{X}$ is expressed by

$$\Delta\dot{\mathbf{X}} = \mathbf{A}\Delta\mathbf{X} \tag{9}$$

The eigenvalue decomposition method can be applied to extract a set of independent linear 1-DOF oscillators from the original system (9), with each one representing an oscillation mode. Diagonalize $\mathbf{A}$ by its modal matrix $\boldsymbol{\phi}$, whose columns are right eigenvectors: $\mathbf{A} = \boldsymbol{\phi}\boldsymbol{\Lambda}\boldsymbol{\phi}^{-1}$. $\boldsymbol{\phi}^{-1}=\boldsymbol{\psi}$, whose rows are left eigenvectors. Define $\mathbf{Y}=\boldsymbol{\psi}\Delta\mathbf{X}$, which includes linearly transformed, decomposed state variables. Amongst $\boldsymbol{\Lambda}$, each conjugate complex pair of eigenvalues, say λ_i and λ_i^*, define one oscillation mode, and the corresponding state variables in $\mathbf{Y}$ are complex-valued since $\boldsymbol{\psi}$ is commonly complex-valued. Then, another transformation $\mathbf{P}$ is adopted [22] to obtain a set of real-valued decomposed state variables, say $\mathbf{Z}$, as in

$$\mathbf{Z} = \mathbf{P}\mathbf{Y} = \mathbf{P}\boldsymbol{\psi}\Delta\mathbf{X} \tag{10}$$

$$\begin{cases} \mathbf{Z} = \left[\mathbf{z}_1^T, \mathbf{z}_2^T, \ldots\right]^T, \ \mathbf{z}_i = \left[\delta_{zi}, \omega_{zi}\right]^T \\ \mathbf{P} = diag\left(\begin{bmatrix} 1 & 1 \\ \lambda_i & \lambda_i^* \end{bmatrix}\right) \end{cases} \tag{11}$$

where $\mathbf{P}\boldsymbol{\psi}$ is the linear transformation to decouple the dynamics of the oscillation modes from $\Delta\mathbf{X}$. $\mathbf{Z}$ contains real-valued linearly decomposed state pairs $\mathbf{z}_i$. Note that $\dot{\delta}_{zi} = \omega_{zi}$, which makes $\mathbf{z}_i$ behaves like an oscillator, i.e. δ_{zi} behaves like an oscillator "angle" and ω_{zi} behaves like "speed". After decomposition, each $\mathbf{z}_i$ corresponds to a pair of conjugate complex eigenvalues as indicated by (11), the imaginary part of which tells the oscillation frequency of the mode. The form of the independent 1-DOF oscillator of each mode can be generalized by:

$$\begin{bmatrix} \dot{\delta}_{zi} \\ \dot{\omega}_{zi} \end{bmatrix} = \begin{bmatrix} 0 & 1 \\ -\sigma_i^2 - \omega_i^2 & 2\sigma_i \end{bmatrix} \begin{bmatrix} \delta_{zi} \\ \omega_{zi} \end{bmatrix} \tag{12}$$

or equivalently:

$$\ddot{\delta}_{zi} + 2\zeta_i\omega_{nat,i}\dot{\delta}_{zi} + \omega_{nat,i}^2\delta_{zi} = 0 \tag{13}$$

where $\lambda_i, \lambda_i^* = \sigma_i \pm j\omega_i$ are a conjugate pair of eigenvalues of (13). ζ_i is the damping ratio and $\omega_{nat,i}$ is the natural frequency. The sensitivity $\partial\sigma_i/\partial k_l$ and $\partial\omega_i/\partial k_l$ are calculated by (15) [7], where ψ_{im} and ϕ_{ni} are entries of $\boldsymbol{\psi}$ and $\boldsymbol{\phi}$. $\partial a_{mn}/\partial k_l$ is the sensitivity of each entry a_{mn} in $\mathbf{A}$ regarding each k_l in $\mathbf{k}$.

$$\zeta_i = -\sigma_i/\omega_{nat,i}, \quad \omega_{nat,i} = \sqrt{\sigma_i^2 + \omega_i^2} \tag{14}$$

$$\frac{\partial\sigma_i}{\partial k_l} + j\frac{\partial\omega_i}{\partial k_l} = \sum_m\sum_n\left(\frac{\partial\sigma_i}{\partial a_{mn}} + j\frac{\partial\omega_i}{\partial a_{mn}}\right) = \sum_m\sum_n \psi_{im}\phi_{ni}\frac{\partial a_{mn}}{\partial k_l} \tag{15}$$

Eq. (13) gives a single oscillator equivalent of the power system regarding the targeted mode. The use of the single oscillator equivalent simplifies the analysis and controller design, since only a 1-DOF oscillator is considered instead of the original high-dimensional power system.

Hereafter, subscript *i* is neglected from (13) for simplicity to focus on the single oscillator equivalent of the targeted mode. The change of $\lambda = \sigma \pm j\omega$ regarding the gains $\mathbf{k}$ can be approximated by:

$$\Delta\sigma + j\Delta\omega = \sum_l \frac{\partial\sigma}{\partial k_l}k_l + j\sum_l \frac{\partial\omega}{\partial k_l}k_l \tag{16}$$

The variation in $\sigma \pm j\omega$ will lead to the variation in ζ and ω_{nat} accordingly. Two assumptions are taken to simplify the analysis, as listed below.

i) $\Delta\omega \approx 0$ is assumed since usually $|\partial\omega/\partial k_l| << |\partial\sigma/\partial k_l|$ and $\Delta\omega << \omega$.

ii) ω_{nat} is assumed to remain unchanged since $\Delta\sigma << \omega_{nat}$.

Hence, (13) becomes (17), which is the power system equivalent representing the targeted mode with $\Delta\sigma$ being considered as the impact of changing $\mathbf{k}$.

$$\ddot{\delta}_z - 2\left(\sigma + \Delta\sigma\right)\dot{\delta}_z + \omega_{nat}^2\delta_z = 0 \tag{17}$$

Remark: The power system equivalent (17) in its form is similar to a linear, harmonic oscillator but has a varying damping coefficient to reflect the control of damping. To address non-linear dynamics in oscillation due to a large disturbance, a damping estimation approach, e.g. the approach in [21], is highly preferred for the proposed damping control method. The equivalent (17) may also be extended to a non-linear form similar to that in [21] but that will increase complexity of the proposed control method in its implementation. For damping control, the varying damping coefficient is most important factor to be modeled by the equivalent, and such an equivalent is found to enable a satisfactory performance under both small and large disturbances.

From the perspective of the damping control system, $\Delta\sigma$ is the total damping by contributions from all PEIRs. Note that the convention of [7] is taken where a negative value of $\Delta\sigma$ means increased damping. Moreover, a negative value of $\partial\sigma/\partial k_l$ means the damping can be increased by increasing the gain k_l, and a bigger $-\partial\sigma/\partial k_l$ means more effective damping improvement at that location. Thus, there are two strategies for DDM to assign k_l to each PEIR:

- *Concurrent distribution strategy*: determine gains k_l by

$$k_l = \left(\frac{\partial\sigma}{\partial k_l}\right)^{-1}\frac{\Delta\sigma}{L} \tag{18}$$

  where sensitivity $\partial\sigma/\partial k_l$ is used as a weighting factor to distribute $\Delta\sigma$ among L participating PEIRs. Thus, it is easy to know that

$$\Delta\sigma = \sum_{l=1}^{L}\left(\frac{\partial\sigma}{\partial k_l}\right)k_l \tag{19}$$

- *Sequential queue strategy*: add PEIRs one by one in the

order of descending $-\partial\sigma/\partial k_l$. Only when a PEIR reaches its power limit, the next one in the queue is used.

B. SISO Transfer Function

As shown in [20], the variation in $\Delta\sigma$ may excite principal and "zero-th order" parametric resonances in δ_z, which makes it more complex to control. Specifically, let $\Delta\sigma = K\cos(\Omega t)$ be a sinusoidal signal with amplitude K and frequency Ω. The principal parametric resonance phenomenon indicates that if $\Omega \approx 2\omega$, the waveform of δ_z exhibits either a periodically varying damping of which the frequency of that periodicity is close to $\sqrt{|(\Omega-2\omega)^2-K^2|}$, or simply a time-variant damping. On the other hand, the "zero-th order" parametric resonance phenomenon indicates that if $\Omega \approx 0$, the waveform of δ_z exhibits periodic varying damping at a frequency close to Ω.

To obtain the transfer function $G(s)$ of the SISO model from input $\Delta\sigma$ to damping ratio ζ_{est}, the "zero-th order" parametric resonance is utilized. Since the frequency of output signal ζ_{est} will be very close to the frequency of the input $\Delta\sigma$ under "zero-th order" parametric resonance, it makes the SISO model behave about linearly. For a simpler transfer function, one way is the use of a low-pass filter in the controller to reduce high frequency components in $\Delta\sigma$ as in Fig. 3. Note that another gain regarding the sensitivity $\partial\zeta/\partial\Delta\sigma$ is also added, which is to analogously convert a signal of damping ratio to a signal of $\Delta\sigma$ that directly impacts the oscillator (17). Based on (14), $\partial\zeta/\partial\Delta\sigma$ is approximated by:

$$\frac{\partial\zeta}{\partial\Delta\sigma} = -\frac{1}{\omega_{nat}} \tag{20}$$

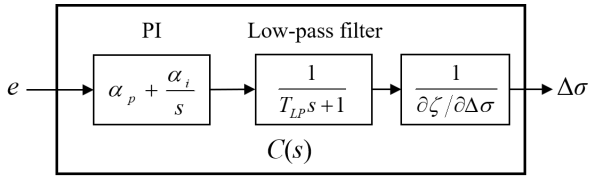

Fig. 3. Controller with a low-pass filter included.

Let the cut-off frequency of the filter be $\omega_{cut} = 1/T_{LP}$. Then, the frequency-response characteristic $G(j\omega)$ of the SISO model in a frequency range of [0, ω_{cut}] can be estimated easily as follows. At any frequency ω_p within the range, inject a sinusoidal signal $\Delta\sigma = K\cos(\Omega t)$ of frequency $\Omega = \omega_p$ and amplitude $K = 1$ into the model (17) and measure the output. How the magnitude and phase angle of the output vary with the input provides approximate $G(j\omega_p)=|G(j\omega_p)|\angle G(j\omega_p)$.

IV. Robust PI Controller

A. Configuration of PI controller

To tune the PI controller, there exists a parameter domain within which any selection of parameters α_p and α_i can stabilize the control system with the control error e eliminated. Such a parameter domain is named the All Stabilizing Parameter Domain (ASPD). Following the PI stabilization method in [28], the ASPD can be analytically determined, within which there can exist infinite selections of α_p and α_i. Thus, more conditions can be added to obtain the optimal selection.

One consideration is that, ideally, the damping ratio of the targeted mode is estimated continuously, but in a practical application, the estimation algorithm may be executed in a discrete manner, e.g. every one second, so $\Delta\sigma$ will be updated at the same frequency. The discontinuity in damping estimates is equivalent to the introduction of disturbances d_i and d_o respectively at both the input and output of the SISO model as indicated in Fig. 4. Hence, the determination of the parameters should have robustness against such disturbances without impacting the time performance of control in quickly stabilizing oscillating generators.

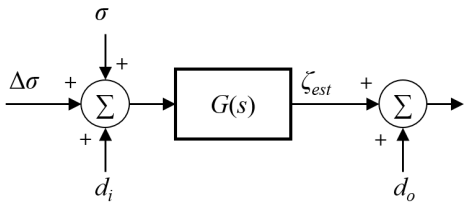

Fig. 4. Disturbances d_i and d_o.

Here, the methodology of [29] is followed to determine α_p and α_i considering both robustness and time performance of the PI controller. For robustness, the influences of d_i and d_o on the estimated damping ratio ζ_{est} are formulated by:

$$\zeta_{est}(s) = T(s)\zeta_{exp}(s) + S(s)G(s)\big(d_i(s)+\sigma(s)\big) - T(s)d_o(s) \tag{21}$$

$$\begin{cases} C(s) = \left(\alpha_p + \dfrac{\alpha_i}{s}\right)\dfrac{1}{T_{LP}s+1} \\ S(s) = \dfrac{1}{1+G(s)C(s)}, \quad T(s) = \dfrac{G(s)C(s)}{1+G(s)C(s)} \end{cases} \tag{22}$$

where $S(s)$ and $T(s)$ are the sensitivity function and complementary sensitivity function, respectively, and their absolute values, $|S(j\omega)|$ and $|T(j\omega)|$, are minimized to respectively reduce the impacts from d_i and d_o. Hence, set the robustness measure as (23). M_{st} can be quickly computed by using the Matlab function *bode*() from the System Identification Toolbox. As suggested in [29], the reasonable values of M_{st} are in a range of 1.2 to 2.0. The smaller M_{st}, the better robustness.

$$M_{st} = \max_{\omega}(|S(j\omega)|, |T(j\omega)|), \qquad \forall\omega\in\mathbb{R} \tag{23}$$

The time performance is characterized by the Integrated Absolute Error (IAE) defined in (24). The smaller *IAE*, the faster stabilization of a perturbed system.

$$IAE = \int_0^\infty |e(t)|\,dt \tag{24}$$

where e is the control error from reference ζ_{exp}.

From [29], it is not always possible to minimize both M_{st} and *IAE* by selecting α_p and α_i for the best robustness and time performance. This can be illustrated by Fig. 5, where the white area is the ASPD on the α_p-α_i plane, the contours of M_{st} are the red curves satisfying $M_{st,i} < M_{st,i+1}$, and the contours of *IAE* are the blue curves with $IAE_i < IAE_{i+1}$. The minimum M^*_{st} and IAE^* are marked by red and blue triangles, respectively. The minima of M_{st} and *IAE* cannot be reached simultaneously since they locate at different locations. One way to uniquely determine α_p and α_i is to make one of the two indices be acceptable for a constraint, not minimal, and minimize the other one. For instance, first select a target value for M_{st}, say $M_{st,tar}$, and then,

find the solution by minimizing *IAE* in the ASPD denoted by Θ. The problem is formulated as:

$$\begin{aligned} \min_{[\alpha_p,\alpha_i]\in\Theta} \quad & IAE \\ s.t. \quad & M_{st} \le M_{st,tar} \end{aligned} \tag{25}$$

Its solution is also visualized in Fig. 5 where $M_{st,tar} = M_{st,1}$. The red area is the feasible domain that meets the constraint. Then, the minimization of *IAE* is to find the contour of *IAE* that is tangent to the feasible domain, which is the contour corresponding to IAE_2. The tangent point p_{opt} is the optimum of (25). Based on the experimental experience, the solution of (25) using the Matlab function *fmincon*() is typically obtained in few seconds, which is fast enough for off-line design.

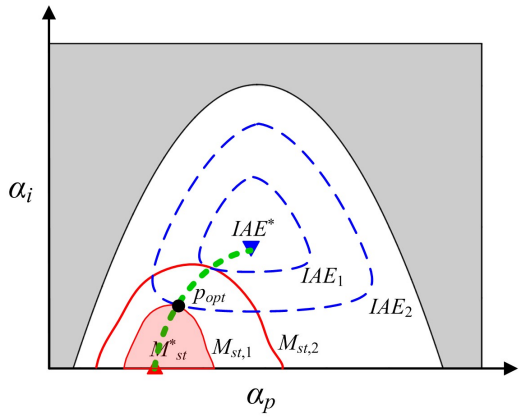

Fig. 5. Trade-off curve and contours of M_{st} and *IAE*.

If different values of $M_{st,tar}$ are selected and the optimum for each value is found, all such optima form a trade-off curve that actually connects the optima of M_{st} and *IAE* on which every point is the so-called Pareto optimal, or in other words, it is impossible to decrease one without increasing the other one. The trade-off curve is illustrated in Fig. 5 as a green dotted curve. The values of α_p and α_i need to be selected on the curve.

Note that the optimization problem in (25) is solved offline or when the system has experienced a significant change in its topology or operating condition. The solved optimal controller parameters are then use for real-time damping control.

B. Implementation of the proposed control method

Algorithms and steps of the proposed damping control method can be aggregated into three functions: 1) damping estimation, 2) PI controller to update $\Delta\sigma$ and DDM to update gains in **k**, 3) changing power outputs of PEIRs by measured $\Delta\boldsymbol{\omega}_C$. In the following, the aforementioned two strategies, i.e. the *concurrent distribution strategy* and *sequential queue strategy*, will be considered, which will respectively implemented in a centralized way and a distributed way.

1) Centralized control

For the targeted mode, its damping ratio is estimated from real-time measurements taken from one or several locations. If phasor measurement unit (PMU)-based wide-area measurements are available and transmitted to the phasor data concentrator (PDC) in the control room, the damping estimation algorithm can be installed at a computer in the control room that can access the PDC. The estimation error on the damping ratio can be viewed as part of disturbance d_o in Fig. 4, and thus, can be mitigated by designing a more robust controller, i.e. setting a small $M_{st,tar}$ and solve the problem (25). The PI controller and DDM are also installed in the control room to update $\Delta\sigma$ and **k** using the *concurrent distribution strategy*. Then, the small amount of data of **k** is transmitted to distributed PEIRs. To avoid communication latency, frequency deviations are measured locally at PEIRs and then used to change their power output according to (2).

2) Distributed control

If communication latency is of concern, a distributed control scheme can be used, in which all functions are implemented at a damping control system connected to each PEIR. For this case, the local damping control system needs to obtain local measurements in order to estimate the damping ratio of the targeted mode. The PI controller and the DMM with each PEIR adopt a *sequential queue strategy* with moderate communication with other PEIRs. This does not require frequent data transmission since it only requires a signal from a PEIR already reaching its power limit to activate the next PEIR in the queue. For instance, assume two PEIRs participate in the proposed damping control method and their gains k_1 and k_2 satisfy $\partial\sigma/\partial k_1 > \partial\sigma/\partial k_2$. Then, let L=1, and from (18), $k_1 = \Delta\sigma / (\frac{\partial\sigma}{\partial k_1})$. When the power output of PEIR 1 reaches its limit and is unable to eliminate $\Delta\sigma$, PEIR 2 is activated using $k_2 = \Delta\sigma / (\frac{\partial\sigma}{\partial k_2})$ based on the remaining $\Delta\sigma$. From the above process, the only communication is the binary activation signal from one PEIR to the other.

Remark: For both centralized and distributed control, it is worthwhile to mention that, if measurement errors are inevitable, the controller design needs to consider more about robustness by solving the optimization problem (25) with a small $M_{st,tar}$. In the case that the estimated real-time damping ratio is much higher than the desired value for the targeted mode, the damping controller can be deactivated.

V. Case Studies on an SMIB System

A. Case Description

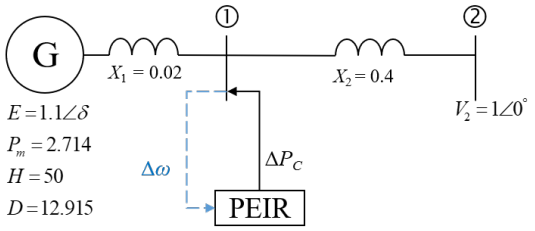

Fig. 6. Diagram of the SMIB system.

In this section, an SMIB system is used to illustrate the basic design procedure of the proposed damping controller. As shown in Fig. 6, Bus 1 is connected to a generator in the classical model and Bus 2 is the infinite bus. The rotor angle δ, speed deviation $\Delta\omega$, inertia H and damping coefficient D are respectively in rad, rad/s, second, and per unit. All the voltage magnitudes, powers and reactances are in per unit. The base

rotor speed is ω_0= 2π×60 rad/s and the base power is 100 MW. The machine is governed by swing equation (26), where P_m is the mechanical power and P_e is the electrical power output. A PEIR is placed near the generator on its transmission path. ΔP_C is the active power injection of the PEIR proportional to its locally measured $\Delta\omega_C$, which is close to $\Delta\omega$ according to (28). The only oscillation mode is given in Table I.

$$\begin{cases} \dot{\delta} = \Delta\omega \\ \dfrac{2H}{\omega_0}\Delta\dot{\omega} = P_m - P_e - D\left(\dfrac{\Delta\omega}{\omega_0}\right) \end{cases} \tag{26}$$

$$\Delta P_C = -k\Delta\omega_C \approx -k\Delta\omega \tag{27}$$

$$V_1 = \frac{1.1X_2\angle\delta + X_1}{X_2 + X_1} \approx 1.1\angle\delta \tag{28}$$

TABLE I. TARGETED MODE FOR DAMPING CONTROLLER DESIGN

Frequency (Hz)	Eigenvalue	Damping ratio (%)
0.2052	– 0.0645 ± 1.2894*i*	5.00

The linearization of (26) gives (29), which can be converted to the form of (17). The eigenvalues and damping ratio ζ of the mode can be computed accordingly.

$$\begin{bmatrix} \Delta\dot{\delta} \\ \Delta\dot{\omega} \end{bmatrix} = \begin{bmatrix} 0 & 1 \\ -1.667 & -3.77k - 0.129 \end{bmatrix} \begin{bmatrix} \Delta\delta \\ \Delta\omega \end{bmatrix} \tag{29}$$

B. Controller design

Because the purpose of this small system study is to demonstrate the detailed controller design rather than the damping estimation algorithm, the true damping ratio is obtained directly from eigenvalues of the state matrix in (29). However, to mimic the time cost for damping estimation, a first order transfer function $1/(T_{mea}\,s + 1)$ is used to receive the true damping ratio and provide the mimicked estimate of damping ratio ζ_{est}. The time constant T_{mea} corresponds to an inevitable time delay (e.g. the time window used by the estimation algorithm) after which a damping ratio change is presented to the damping controller. Also, the same simplification is also considered for the control model to approximate transfer function $G(s)$ by (30), where the variation in the damping ratio ζ is determined by its sensitivity regarding $\Delta\sigma$. By doing so, the performance of the controller itself can be analyzed excluding errors caused by the damping estimation algorithm or the "zero-th order" parametric resonances. Here, assume T_{mea} = 3 s.

$$G(s) = \frac{\partial\zeta}{\partial\Delta\sigma}\frac{1}{T_{mea}s+1} = -\frac{0.774}{Ts+1} \tag{30}$$

For the low-pass filter in Fig. 3, the cut-off frequency of is set as ω_{cut} = 2π×0.3 rad/s, so $T_{LP} = 1/\omega_{cut}$ = 0.53. $S(s)$ and $T(s)$ are determined from (22). Now, only the parameters α_p and α_i of the PI controller need to be determined via the consideration of M_{st} and *IAE*. Since ASPD is a large domain for this case, a subdomain is considered which contains the domain of $M_{st} \le 2$. The trade-off curve and the contours of M_{st} and *IAE* are depicted in Fig. 7. The trade-off curve corresponds to $1 \le M_{st} \le 2.41$ and $0.68 \le IAE \le 301.4$.

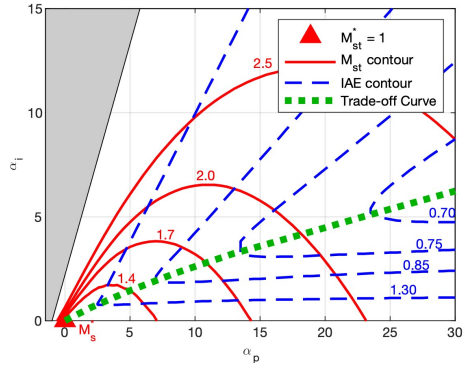

Fig. 7. Trade-off curve and contours of M_{st} and *IAE*: SMIB system.

The control model containing an SISO equivalent in Fig. 1 is used for the controller design. To show whether it can credibly reflect the dynamics of the power system equipped with the proposed controller, consider a step input to both the power system and control model. Their responses are compared using the following test scenario, in which the system maintains its damping ratio at 5% until a disturbance decreases its damping ratio. For the test on the power system, first deactivate the proposed damping controller, and then, decrease D to 12 and P_m to 2.65 to allow more sustained oscillation. Based on the simulation result, without the proposed controller, the damping ratio drops to 3.60% after D and P_m is decreased. Then, re-activate the proposed controller with ζ_{exp}=5%. Note that the input $\Delta\sigma$ is updated every 0.5 sec. For the test on the control model, to stimulate the same test scenario as the power system, ζ_{exp} is initially set as 3.60% and then has a step change to 5%.

Three points on the trade-off curve, [3.4281, 1.0427], [6.7381, 1.8829] and [11.7281, 2.9817], are selected for [α_p, α_i], which are corresponding to [M_{st}, *IAE*] = [1.3, 1.1266], [1.5, 0.8582], and [1.75, 0.7652], respectively. The comparisons are given in Fig. 8. For the sake of convenience, the responses of the damping ratio are realigned such that t = 0 s corresponds to the moment of the step change.

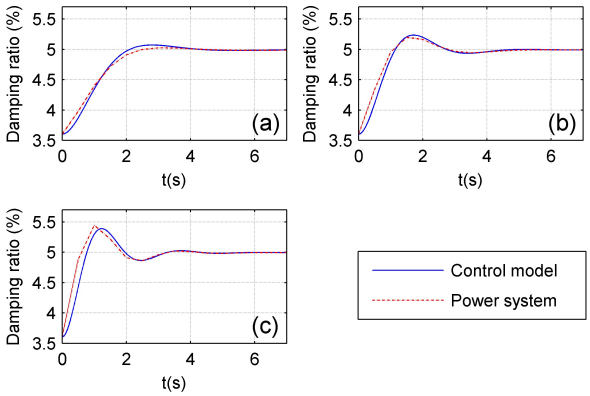

Fig. 8. Comparison: (a) [α_p, α_i] = [3.4281, 1.0427], (b) [α_p, α_i] = [6.7381, 1.8829], (c) [α_p, α_i] = [11.7281, 2.9817].

The results from the control model and the power system agree well for small M_{st}, but become more different when M_{st}

becomes larger. Hence, it is recommended to set a small M_{st} so that the control model reflects the real scenario.

C. Tests on Scenarios

In this section, two more scenarios are added to test the performance of the proposed controller against a disturbance occurring at t = 15 s, named **Scenarios 1, 2** (i.e. the scenario in section V.B) **and 3**, which respectively decreases D to 12, 10, and 8 at t=15 s. Meanwhile, P_m is decreased to 2.65 for all the scenarios. If there was no damping control, the damping ratio would drops to 3.60%, 3.00% and 2.40%, respectively. Three groups of values of [α_p, α_i] are [3.4281, 1.0427], [6.7381, 1.8829] and [11.7281, 2.9817], which respectively correspond to [M_{st}, IAE] = [1.3, 1.1266], [1.5, 0.8582], and [1.75, 0.7652]. In tests, the damping controller is activated all the time.

Note that the damping ratio is calculated and $\Delta\sigma$ is updated for every 0.5 second. The comparisons of those three groups of parameters are given in Fig. 9 for **Scenarios 1-3**, respectively.

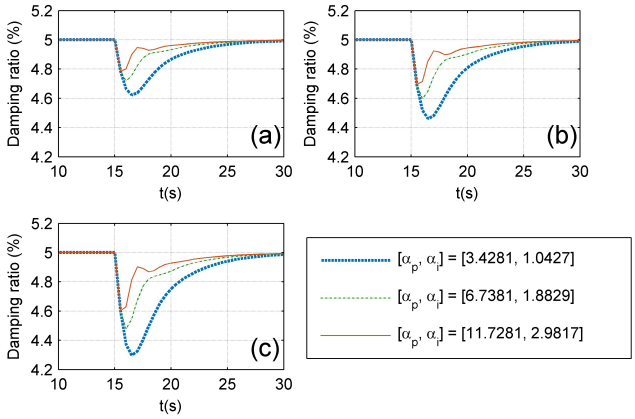

Fig. 9. Performance of damping controller: (a) **Scenario 1**, (b) **Scenario 2,** (c) **Scenario 3**.

From the results, all three groups of parameters can control the damping ratio to 5% for three scenarios. Their comparisons show that the [α_p, α_i] with the smallest IAE can control the damping ratio best because it has the largest amplitude of active power outputs.

Damping control and improvement by the proposed controller can be reflected from the power and rotor angle waveforms. Take [α_p, α_i] = [3.4281, 1.0427] as an example and compare the results of the **Scenario 1** with and without the damping controller. Within the interval of t = 15 to 60 s, the relative rotor angle $\Delta\delta$ regarding the stable operating condition, the PEIR power output ΔP_C, and the variation of generator power output ΔP_e are compared in Fig. 10, Fig. 11, and Fig. 12, respectively. It can be observed that the oscillations in the rotor angle and generator power output are diminished by damping control from the PEIR as reflected from ΔP_C starting from t=15 s. The amplitude of ΔP_C is small compared to the variation of power output of the generator ΔP_e. As the damping ratio is approaching the expected value, ΔP_C gradually vanishes. Because of an approximate symmetry in the waveform of ΔP_C, the net energy change of the PEIR is also small. This means that the PEIR participating in the proposed damping control method does not need to have a large size in its power or energy.

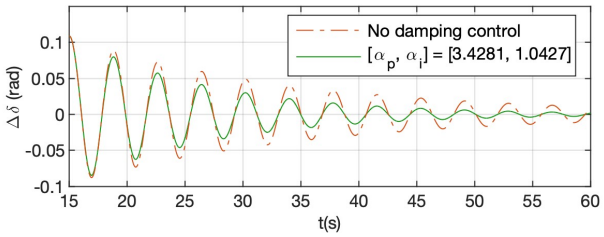

Fig. 10. Relative rotor angle, $\Delta\delta$.

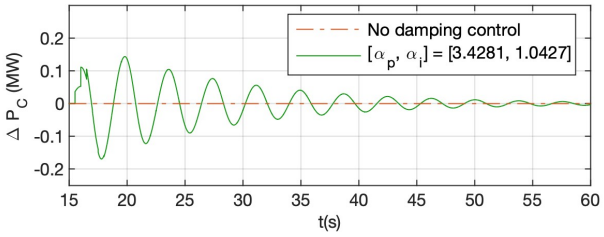

Fig. 11. PEIR power output, ΔP_C.

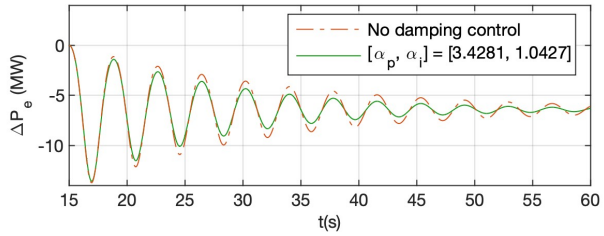

Fig. 12. Variation of generator power output, ΔP_e.

D. Comparison with open-loop damping control

The proposed damping controller is able to control the damping ratio accurately toward an expected value thanks to its closed-loop, feedback control mechanism. Here, it is compared to an open-loop damping control method in [14], which pre-determines a fixed gain to increase the damping ratio by an expected value but does not utilize any feedback signal on real-time damping with the control. Thus, there is a risk not to meet the expected damping ratio under some disturbance. For instance, by considering the **Scenarios 1** and **2**, it is determined k = 0.0176 for ζ_{exp}=5%. However, when the **Scenario 3** happens, the damping ratio using an open-loop control method in [14] falls to 4.39%. Therefore, closed-loop feedback damping control can more accurately control the damping ratio to an expected value under unanticipated disturbances.

VI. Case Studies on the NPCC System

A. Controller Design

The proposed design procedure is validated on an NPCC 140-bus 48-generator test system. The system data are the same as in [30] except that one line is added between Buses 13 and 7, with the impedance to be j0.0028 (pu). The one-line diagram is shown in Fig. 13.

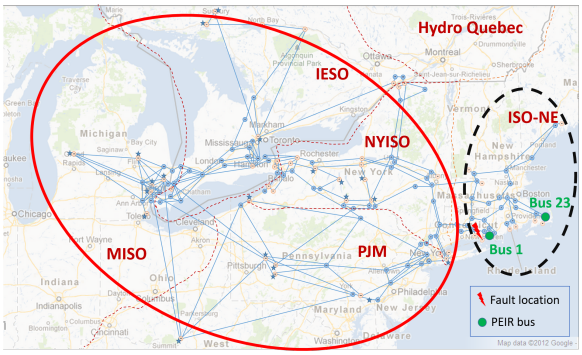

Fig. 13. One-line diagram of the NPCC 140-bus power system and the two groups that swing against each other under the 0.6 Hz mode [23].

A 0.62 Hz mode is targeted and controlled by the proposed damping controller. It is a critical inter-area mode that causes the generators in the ISO-NE region to oscillate against other regions, as indicated from the mode shape [23] and shown in Fig. 13. The expected damping ratio is ζ_{exp} = 3%. In Table II, the pair of eigenvalues on this targeted mode is obtained from the linearized system model, and the damping ratio is found to be very close to the expected 3% without any disturbance. This case study aims to control its damping ratio accurately at 3% even under a disturbance or topological change of the system.

Buses 1 and 23 are assumed to have PEIRs installed as marked in Fig. 13. Ignore fast dynamics of PEIRs and assume $\Delta\mathbf{P}_C = -diag(\mathbf{k})\Delta\boldsymbol{\omega}_C$. For each bus, $0 \le k_l \le 200$. From the sensitivity $\partial\sigma/\partial k_l$ in Table III, Bus 23 is better to control damping of the 0.62 Hz mode. In addition, at the early stage of the disturbance, a well-damped 0.53 Hz mode will also be excited with a damping ratio of 8.95%. Its sensitivity $\partial\sigma/\partial k_l$ is also given in Table III. The PEIRs increase damping of both modes.

TABLE II. TARGETED MODE FOR DAMPING CONTROLLER DESIGN

Frequency (Hz)	Eigenvalues	Damping ratio (%)
0.62	$-0.1175 \pm 3.8872i$	3.02

TABLE III. SENSITIVITY

Bus	Mode 0.62 Hz	Mode 0.53 Hz
1	-1.16×10^{-4}	-2.83×10^{-5}
23	-2.38×10^{-4}	-3.78×10^{-5}

The single oscillator equivalent for the targeted mode and the transfer function of $G(s)$ are given in (31). Note that ω_{cut} = 2π×0.3 rad/s is selected to meet the assumption of "zero-th order" parametric resonance. The cut-off frequency of the low-pass filter is also set as ω_{cut} = 2π×0.3 rad/s, i.e. $T_{LP} = 1/\omega_{cut}$ = 0.53. $S(s)$ and $T(s)$ are determined following (22).

$$\begin{cases} \ddot{\delta}_z - 2\left(-0.1174 + \Delta\sigma\right)\dot{\delta}_z + 15.1243\delta_z = 0 \\ G(s) = -\dfrac{0.1774s^2 - 0.0372s + 0.960}{s^3 + 3.338s^2 + 5.788s + 3.975} \end{cases} \tag{31}$$

Now, only the parameters α_p and α_i of the PI controller need to be determined. The trade-off curve and the contours of M_{st} and IAE are depicted in Fig. 14. The trade-off curve corresponds to $1 \le M_{st} \le 1.75$ and $2.15 \le IAE \le 82.71$.

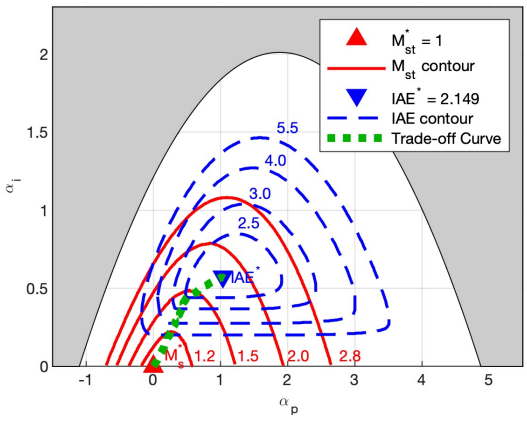

Fig. 14. Trade-off curve and contours of M_{st} and IAE: NPCC system.

The credibility of the control model in Fig. 1 is investigated in terms of reflected dynamics of the power system equipped with the proposed controller. Similar to the SMIB case, a step input is considered to both the system and control model and their responses are compared. Settings of the power system and control model are as follows. On the NPCC system, first deactivate the proposed damping controller, and excite an oscillation by a permanent three-phase fault added to Bus 13 and cleared after 0.125 s by disconnecting the line 13-7. From the simulation result, without the proposed controller, the damping ratio of the targeted mode drops to 0.92% with the post-fault system. Then, re-activate the proposed controller with ζ_{exp}=3%. Note that the input $\Delta\sigma$ is updated every 0.5 sec. For the control model, to ensure the same test scenario as that with the power system, ζ_{exp} is initially 0.92% and then has a step change to 3%. On the NPCC system, the first several seconds are ignored to skip the nonlinear fault-on response of the system, which can introduce errors to any damping estimation method. Handling of those data is discussed in the next subsection.

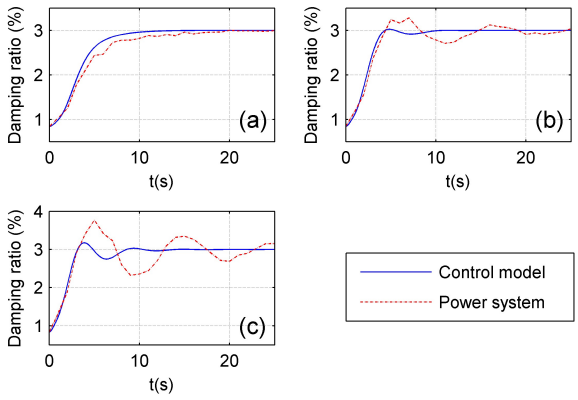

Fig. 15. Comparison: (a) [α_p, α_i] = [0.3251, 0.3172], (b) [α_p, α_i] = [0.6518, 0.4742], (c) [α_p, α_i] = [1.0557, 0.5623].

Three points on the trade-off curve, [0.3251, 0.3172], [0.6518, 0.4742] and [1.0557, 0.5623], are selected for [α_p, α_i], which are corresponding to [M_{st}, IAE] = [1.3, 3.479], [1.5, 2.333], and [1.75, 2.149], respectively. The comparisons are given in Fig. 15. For the sake of convenience, the responses of the damping ratio are realigned such that t = 0 s corresponds to

the moment of the step change. The results from the control model and the power system simulation agree well when M_{st} is small, and become less consistent when M_{st} becomes larger. Hence, it is recommended to set M_{st} to be a small value, such that the control model properly reflects the real scenario.

Finally, the case of $[\alpha_p, \alpha_i] = [1.0557, 0.5623]$ is used to show the accuracy of the approximation from (7) to (8) by neglecting the derivative of $\Delta\mathbf{P}_C$. The true $\Delta\boldsymbol{\omega}_C$ and the approximated $\Delta\boldsymbol{\omega}_C$ are compared for Buses 1 and 23, and the results are shown in Fig. 16. Note that only the PEIR at Bus 23 has variation in its parameter k_l since it is more effective according to the sensitivity $\partial\sigma/\partial k_l$. There exists an observable difference between the true $\Delta\boldsymbol{\omega}_C$ and the approximated $\Delta\boldsymbol{\omega}_C$ for Bus 23, which is caused by neglecting the derivative of $\Delta\mathbf{P}_C$, while eq. (8) is accurate for Bus 1 where there is no variation in the power output. Since the approximated $\Delta\boldsymbol{\omega}_C$ still follows the true $\Delta\boldsymbol{\omega}_C$, such error is acceptable in terms of controller design.

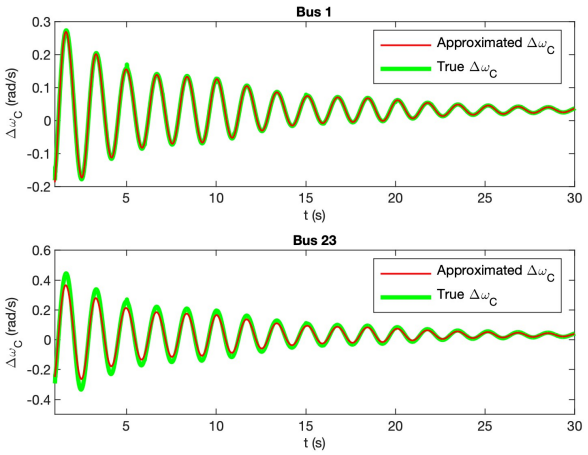

Fig. 16. Comparison of true and approximated $\Delta\boldsymbol{\omega}_C$.

B. *Test on a More Practical Scenario*

In this section, a more practical scenario is considered to test the performance of the proposed controller against a disturbance occurring in the middle of the testing period. At $t = 30$ s, a permanent three-phase fault is added at Bus 13 and cleared respectively at its critical clearing time (CCT) = 0.125 s and 0.5CCT = 0.0625 s by disconnecting the line 13-7. Three groups of parameters are selected for $[\alpha_p, \alpha_i]$, i.e. [0.3251, 0.3172], [0.6518, 0.4742] and [1.0557, 0.5623], which respectively correspond to $[M_{st}, IAE]$ = [1.3, 3.479], [1.5, 2.333], and [1.75, 2.149]. The damping controller is activated all the time.

When the controller keeps operating under an unanticipated disturbance, it may receive both fault-on and post-fault measurements. Thus, two facts can affect damping control performance. First, the measurements do not present a single autonomous dynamical system since the system is undergoing a switch. Thus, damping estimated on the measurements containing responses before and after a switch is not reliable. For instance, many damping estimation algorithms may report a non-oscillatory mode due to misidentification of a real eigenvalue. Second, the response of the post-fault system often exhibits severe nonlinearity, so ringdown data right after a large disturbance are often discarded by default in most of commercial damping estimation tools such as the Prony's analysis tool with the TSAT software by Powertech Labs [31]. Thus, a robust damping estimation method less affected by appearances of switches and nonlinearities in data is preferred for the proposed control method.

The remedy selected in this paper to address two aforementioned facts is to use the nonlinear oscillator fitting based damping ratio estimation approach in [21]. This estimation approach can better deal with nonlinear oscillations in the early stage of a post-fault period and is insensitive to the selection of the length of measuring time window so as to be more accurate and robust than other existing methods, as demonstrated from flatter damping ratio curves it gives under large disturbances. Also, the approach can be applied to the data containing faults. Since it is based on online identification of a nonlinear oscillator from the extracted modal response data on the targeted mode, the identified oscillator and its damping adaptively change with the data as well as the switches of the system. In [21], this estimation approach is tested on historical data from the 2011 Southwest Blackout that contain several events and switches including generator trips. The approach provides meaningful results.

Note that the length of the measuring time window is selected as 3 seconds. The damping ratio is estimated and updated for every 0.5 second. The comparisons of those three groups of parameters are given in Fig. 17 when the fault is cleared at the CCT, and in Fig. 18 when the fault is clear at 0.5 CCT. The results show that all the three groups of $[\alpha_p, \alpha_i]$ can eliminate damping ratio deviations. The comparisons during the period of $t = 35$ to 50 s show that a group of $[\alpha_p, \alpha_i]$ with smaller IAE can eliminate deviations much faster. For instance, in Fig. 18, using [1.0557, 0.5623] for $[\alpha_p, \alpha_i]$ enables about 5 seconds faster control of the damping ratio to 3% than using [0.3251, 0.3172].

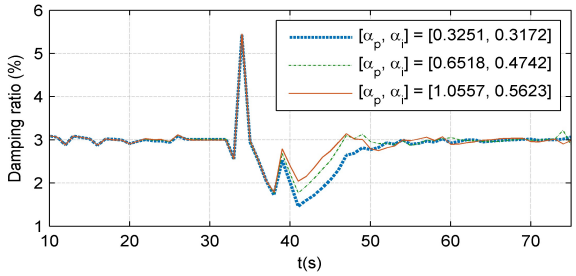

Fig. 17. Performance of damping controller: fault cleared at CCT.

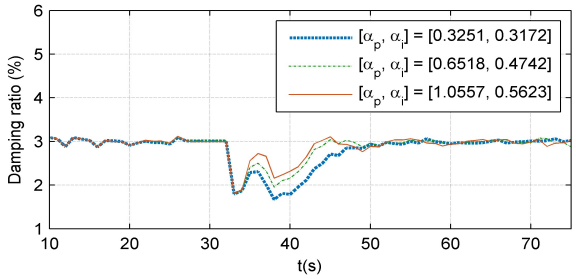

Fig. 18. Performance of damping controller: fault cleared at 0.5 CCT.

Fig. 17 shows variations in the measured damping ratio. At

t=34 s, the sudden increase is mainly caused by the system nonlinear response. As explained in [21], when fault is cleared at about its CCT, the modal response of the targeted mode may exhibit a sudden decay in the waveform of the data, which is interpreted as large damping by most of damping estimation algorithms. Then, at t=39 s, there is another observed increase, due to the fact that, if the control signal $\Delta\sigma$ contains harmonics instead of being a clean sinusoidal wave, the system response will exhibit an uneven damping ratio. If such increase is viewed as a part of disturbance d_i in Fig. 1, one may enhance the robustness against such disturbance by choosing a small M_{si} in the determination of α_p and α_i.

Damping improvement by the proposed controller is reflected from the power and rotor angle waveforms. Take the controller with [α_p, α_i] = [0.6518, 0.4742] as an example and compare the results on the case of 0.5CCT. Within the interval of t = 30 to 75 s, the rotor angle difference between generators 28 and 5, $\Delta\delta_{28\text{-}5}$, the power output of the PEIR at Bus 23, ΔP_{C23}, and the power output of generator 5, P_{e5}, are compared in Fig. 19, Fig. 20, and Fig. 21, respectively. Based on the mode shape analysis as in [21], the mode is highly observable from measurements of generators 28 and 5. The oscillations in the rotor angle and generator power output are diminished by damping control as reflected from ΔP_{C23}. The amplitude of ΔP_{C23} is small compared to P_{e5}. As the damping ratio is approaching the expected value, ΔP_{C23} gradually vanishes. Same as the SMIB system study, this NPCC case study also confirms that each PEIR participating in the proposed damping control method does not need to have a large size in power or energy.

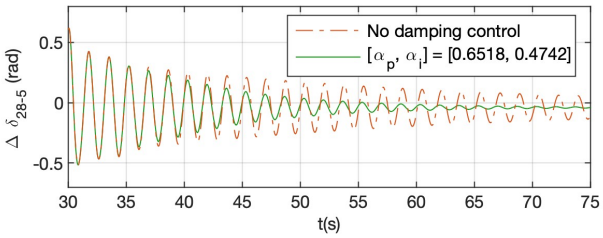

Fig. 19. Rotor angle difference between generator 28 and 5, $\Delta\delta_{28\text{-}5}$.

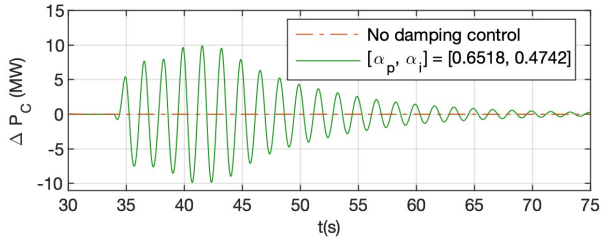

Fig. 20. Power output of PEIR at Bus 23, ΔP_{C23}.

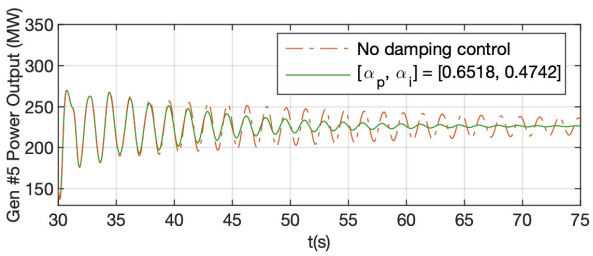

Fig. 21. Power output of generator 5, P_{e5}.

VII. Conclusions

A direct feedback control method has been proposed for real-time damping control of a power system under both small and large disturbances. The feedback control system applies a PI controller to an SISO model on the power system, which approximates the modal dynamics of the targeted mode based on a single oscillator equivalent. The optimal parameters of the PI controller are determined by considering both the robustness and time performance. Simulation results on the SMIB system and the 48-machine NPCC system has validated the effectiveness of the proposed damping controller.

The proposed controller employs an NMD-based damping estimation algorithm and hence is promising for damping control with more than one modes because the NMD method decomposes a power system regarding multiple nonlinear oscillation modes for stability analysis and control purposes under both small and large disturbances. Accordingly, damping of multiple models can be estimated in real time [21]. Future works include but not limited to: *i*) the optimal placement of damping controllers, and *ii*) application of the proposed damping controller to multiple modes.

Appendix A

Detailed steps to derive eq. (3) are following.

First, there are

$$\Delta\mathbf{P}_e + j\Delta\mathbf{Q}_e = \Delta(\mathbf{E}'\mathbf{I}_G^*) = \overline{\mathbf{E}}'\Delta\mathbf{I}_G^* + \overline{\mathbf{I}}_G^*\Delta\mathbf{E}' \tag{32}$$

$$\Delta\mathbf{P}_C + j\Delta\mathbf{Q}_C = \Delta(\mathbf{V}_C\mathbf{I}_C^*) = \overline{\mathbf{V}}_C\Delta\mathbf{I}_C^* + \overline{\mathbf{I}}_C^*\Delta\mathbf{V}_C \tag{33}$$

where bars indicate values at a stable condition. The network equations on $\mathbf{E}'$, $\mathbf{I}_G$, $\mathbf{V}_C$ and $\mathbf{I}_C$ are obtained by Kron reduction:

$$\begin{bmatrix}\mathbf{I}_G\\ \mathbf{I}_C\end{bmatrix} = \begin{bmatrix}\mathbf{Y}_{EE} & \mathbf{Y}_{EC}\\ \mathbf{Y}_{CE} & \mathbf{Y}_{CC}\end{bmatrix}\begin{bmatrix}\mathbf{E}'\\ \mathbf{V}_C\end{bmatrix} \tag{34}$$

Next, substitute (34) into (32) and (33) to eliminate $\mathbf{I}_G$ and $\mathbf{I}_C$ and then reorganize the result by block matrices $\mathbf{K}_{ij}$'s:

$$\begin{bmatrix}\Delta\mathbf{P}_e\\ \Delta\mathbf{Q}_e\\ \Delta\mathbf{P}_C\\ \Delta\mathbf{Q}_C\end{bmatrix} = \begin{bmatrix}\mathbf{K}_{11} & \mathbf{K}_{12} & \mathbf{K}_{13} & \mathbf{K}_{14}\\ \mathbf{K}_{21} & \mathbf{K}_{22} & \mathbf{K}_{23} & \mathbf{K}_{24}\\ \mathbf{K}_{31} & \mathbf{K}_{32} & \mathbf{K}_{33} & \mathbf{K}_{34}\\ \mathbf{K}_{41} & \mathbf{K}_{42} & \mathbf{K}_{43} & \mathbf{K}_{44}\end{bmatrix}\begin{bmatrix}\Delta\mathbf{E}'_x\\ \Delta\mathbf{E}'_y\\ \Delta\mathbf{V}_{Cx}\\ \Delta\mathbf{V}_{Cy}\end{bmatrix} \tag{35}$$

Here, subscripts x and y indicates real and imaginary parts of a phasor in non-rotating coordinates, respectively. From the last two equations of (35):

$$\begin{bmatrix}\Delta\mathbf{V}_{Cx}\\ \Delta\mathbf{V}_{Cy}\end{bmatrix} = \begin{bmatrix}\mathbf{K}_{33} & \mathbf{K}_{34}\\ \mathbf{K}_{43} & \mathbf{K}_{44}\end{bmatrix}^{-1}\left(\begin{bmatrix}\Delta\mathbf{P}_C\\ \Delta\mathbf{Q}_C\end{bmatrix} - \begin{bmatrix}\mathbf{K}_{31} & \mathbf{K}_{32}\\ \mathbf{K}_{41} & \mathbf{K}_{42}\end{bmatrix}\begin{bmatrix}\Delta\mathbf{E}'_x\\ \Delta\mathbf{E}'_y\end{bmatrix}\right) \tag{36}$$

Substitute (36) into the first two equations of (35) to eliminate $\Delta\mathbf{V}_{Cx}$ and $\Delta\mathbf{V}_{Cy}$. Thus, $\Delta\mathbf{P}_e$ and $\Delta\mathbf{Q}_e$ can be expressed by:

$$\begin{bmatrix}\Delta\mathbf{P}_e\\ \Delta\mathbf{Q}_e\end{bmatrix} = \begin{bmatrix}\boldsymbol{\kappa}_{11} & \boldsymbol{\kappa}_{12} & \boldsymbol{\kappa}_{13} & \boldsymbol{\kappa}_{14}\\ \boldsymbol{\kappa}_{21} & \boldsymbol{\kappa}_{22} & \boldsymbol{\kappa}_{23} & \boldsymbol{\kappa}_{24}\end{bmatrix}\begin{bmatrix}\Delta\mathbf{E}'_x\\ \Delta\mathbf{E}'_y\\ \Delta\mathbf{P}_C\\ \Delta\mathbf{Q}_C\end{bmatrix} \tag{37}$$

where $\boldsymbol{\kappa}_{ij}$'s are resulting block matrices.

Finally, since $\Delta\mathbf{E}'_x$ and $\Delta\mathbf{E}'_y$ can be considered as linear combinations of $\Delta\boldsymbol{\delta}$ and their d-q axis components, $\Delta\mathbf{E}'_d$ and $\Delta\mathbf{E}'_q$, in the rotating coordinates, and also we note that $\Delta\mathbf{Q}_C = 0$, eq. (3) can be derived from (37).

REFERENCES

[1] Y. Wang, J. Meng, X. Zhang, L. Xu, "Control of PMSG-based wind turbines for system inertial response and power oscillation damping," *IEEE Trans. Sustain. Energy*, vol. 6, no. 2, pp. 565–574, Apr. 2015.

[2] Y. Liu, Y. Liu, J. R. Gracia, T. J. King, "Oscillation damping contributions of variable-speed wind generators in the Eastern Interconnection (EI)," *2014 IEEE PES General Meeting*, National Harbor, 2014.

[3] C. Loutan et al., "Demonstration of essential reliability services by a 300-MW solar photovoltaic power plant," Nat. Renewable Energy Lab., Golden, CO, USA, Tech. Rep. NREL/TP-5D00-67799, 2017.

[4] R. K. Varma, M. Akbari, "Simultaneous Fast Frequency Control and Power Oscillation Damping by Utilizing PV Solar System as PV-STATCOM," *IEEE Trans. Sustain. Energy*, vol. 11, no. 1, pp. 415-425, Jan. 2020.

[5] Y. Zhu, B. Wang, K. Sun, "Damping control for power systems using energy storage," *29th Chinese Control and Decision Conference*, Chongqing, 2017.

[6] H. Pulgar-Painemal, Y. Wang, H. Silva-Saravia, "On inertia distribution, inter-area oscillations and location of electronically-interfaced resources," *IEEE Trans. Power Syst.*, vol. 33, no. 1, pp. 995–1003, Jan. 2018.

[7] P. Kundur, *Power System Stability and Control*. New York: McGraw-Hill, 1994.

[8] Aboul-Ela, A. Sallam, J. McCalley, A. Fouad, "Damping controller design for power system oscillations using global signals," *IEEE Trans. Power Syst.*, vol. 11, no. 2, pp. 767–773, May 1996.

[9] Y. Zhang, A. Bose, "Design of wide-area damping controllers for interarea oscillations," *IEEE Trans. Power Syst.*, vol. 23, no. 3, pp. 1136–1143, Aug. 2008.

[10] I. Kamwa, R. Grondin, V. Hebert, "Wide-area measurement based stabilizing control of large power systems—A decentralized/hierarchical approach," *IEEE Trans. Power Syst.*, vol. 16, pp. 136–153, Feb. 2001.

[11] D. P. Ke, C. Y. Chung, Y. Xue, "An Eigenstructure-Based Performance Index and Its Application to Control Design for Damping Inter-Area Oscillations in Power Systems," *IEEE Trans. Power Syst.*, vol. 26, no. 4, pp. 2371-2380, Nov. 2011.

[12] Q. Mou, H. Ye, Y. Liu, "Nonsmooth Optimization-Based WADC Tuning in Large Delayed Cyber-Physical Power System by Interarea Mode Tracking and Gradient Sampling," *IEEE Trans. Power Systems*, vol. 34, no. 1, pp. 668-679, Jan. 2019.

[13] Y. Zhu, C. Liu, B. Wang, K. Sun, "Damping control for a target oscillation mode using battery energy storage," *J. Modern Power Syst. Clean Energy*, vol. 6, pp. 833–845, 2018.

[14] Y. Zhu, C. Liu, K. Sun, D. Shi, Z. Wang, "Optimization of battery energy storage to improve power system oscillation damping," *IEEE Trans. Sustain. Energy*, vol. 10, no. 3, pp. 1015–1024, Jul. 2019.

[15] B. C. Pal et al., "Robust damping controller design in power systems with superconducting magnetic energy storage devices," *IEEE Trans. Power Syst.*, vol. 15, no. 1, pp. 320–325, Feb. 2000.

[16] S. Y. Ruan, G. J. Li, B. T. Ooi, Y. Z. Sun, "Power system damping from real and reactive power modulations of voltage source converter station," *IET Gener. Transm. Distrib.*, vol. 2, no. 3, pp. 311–320, 2008.

[17] X. Sui, Y. Tang, H. He, J. Wen, "Energy-storage-based low-frequency oscillation damping control using particle swarm optimization and heuristic dynamic programming," *IEEE Trans. Power Syst.*, vol. 29, no. 5, pp. 2539–2548, Sep. 2014.

[18] J. Ma, et al, "Adaptive Damping Control of Inter-Area Oscillations Based on Federated Kalman Filter Using Wide Area Signals," *IEEE Trans. Power Syst.*, vol. 28, no. 2, pp. 1627-1635, May 2013.

[19] H. Silva-Saravia, et al, "Adaptive Coordination of Damping Controllers for Enhanced Power System Stability," *IEEE Open Access Journal of Power and Energy*, vol. 7, pp. 265-275, 2020.

[20] X. Xu, K. Sun, "On Periodical Damping Ratio of a Controlled Dynamical System with Parametric Resonances," arXiv:2012.02932, Dec. 2020.

[21] X. Xu, W. Ju, B. Wang, K. Sun, "Real-time Damping Estimation on Nonlinear Electromechanical Oscillation," *IEEE Trans. Power Syst.*, Dec. 2020. (*Early Access*).

[22] B. Wang, K. Sun, W. Kang, "Nonlinear Modal Decoupling of Multi-Oscillator Systems with Applications to Power Systems," *IEEE Access*, vol. 6, pp. 9201-9217, 2018.

[23] X. Xu, B. Wang, K. Sun, "Initial Study of the Power System Stability Boundary Estimated from Nonlinear Modal Decoupling," *IEEE PES Powertech*, June 23-27, 2019, Milano, Italy

[24] B. Wang, K. Sun, X. Xu, "Nonlinear modal decoupling based power system transient stability analysis," *IEEE Trans. Power Syst.*, vol. 34, no. 6, pp. 4889-4899, Jun. 2019.

[25] T. Xia, Z. Yu, K. Sun, D. Shi, Z. Wang, "Extended Prony Analysis on Power System Oscillation under a Near-Resonance Condition," *IEEE PES General Meeting*, 2020.

[26] Y. Chompoobutrgool, L. Vanfretti, "Identification of Power System Dominant Inter-Area Oscillation Paths," *IEEE Trans. Power Syst.*, vol. 28, no. 3, pp. 2798-2807, Aug. 2013.

[27] F. Milano, Á. Ortega, "Frequency Divider," *IEEE Trans. Power Syst.*, vol. 32, no. 2, pp. 1493-1501, March 2017.

[28] G. J. Silva, A. Datta, S. P. Bhattacharyya, "PI Stabilization of Delay-Free Linear Time-Invariant Systems" in *PID controllers for time-delay systems*. Springer Science & Business Media, 2007.

[29] O. Garpinger, et al, "Performance and robustness trade-offs in PID control", *J. Process Control*, vol. 24, no. 5, pp. 568-577, 2014.

[30] J. Chow, G. Rogers, *User manual for power system toolbox*, Version 3.0, 2008.

[31] L. Wang, "Techniques for high performance analysis of transient stability," *IEEE PES General Meeting*, San Diego, CA, 2012.

Xin Xu (S'15) received the Ph.D. degree in electrical engineering from University of Tennessee in 2020. Before that, he received the B.E. and M.E. degree in electrical engineering from Shandong University in 2013 and 2016, respectively. He is now an engineer in electric transmission operations engineering with Dominion Energy. His main research interests include data analytics application in power systems, and nonlinear system dynamics, stability assessment and control.

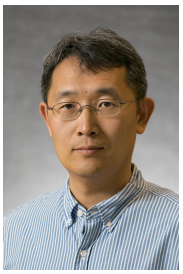

Kai Sun (M'06–SM'13) received the B.S. degree in automation in 1999 and the Ph.D. degree in control science and engineering in 2004 both from Tsinghua University, Beijing, China. He is an associate professor at the Department of EECS, University of Tennessee, Knoxville, USA. He was a project manager in grid operations and planning at the EPRI, Palo Alto, CA from 2007 to 2012. Dr. Sun serves in the editorial boards of IEEE Transactions on Power Systems, IEEE Transactions on Smart Grid, IEEE Access and IEEE Open Access Journal of Power and Energy.